Journal of Mechanics in Medicine and Biology

An alternative to periodic homogenization for dentin elastic stiffness

CHLOE ARSON
School of Civil & Environmental Engineering, Georgia Institute of Technology
790 Atlantic Drive, Atlanta, GA 30332-0355, USA
chloe.arson@ce.gatech.edu
http://arson.ce.gatech.edu

YANNICK YASOTHAN
Laboratoire MSSMat (CNRS), Centrale Supélec, Université Paris-Saclay
Plateau de Moulon, 3 rue Joliot Curie, Gif-sur-Yvette, 91192, France
yannick.yasothan@gadz.org

ROMAIN JEANNERET
Laboratoire MSSMat (CNRS), Centrale Supélec, Université Paris-Saclay
Plateau de Moulon, 3 rue Joliot Curie, Gif-sur-Yvette, 91192, France
romain.jeanneret-dit-grosjean@student.ecp.fr

AURELIE BENOIT
Laboratoire URB2I, Faculté de chirurgie dentaire, Université Paris-Descartes
1, rue Maurice Arnoux, 92120 Montrouge, France
aurelie.benoit@parisdescartes.fr

NICOLAS ROUBIER
Laboratoire MSSMat (CNRS), Centrale Supélec, Université Paris-Saclay
Plateau de Moulon, 3 rue Joliot Curie, Gif-sur-Yvette, 91192, France
nicolas.roubier@centralesupelec.fr

ELSA VENNAT
Laboratoire MSSMat (CNRS), Centrale Supélec, Université Paris-Saclay
Plateau de Moulon, 3 rue Joliot Curie, Gif-sur-Yvette, 91192, France
URB2i, Université Paris Descartes, Montrouge, France
elsa.vennat@centralesupelec.fr

Received (Day Month Year)
Accepted (Day Month Year)

Dentin, the main tissue of the tooth, is made of tubules surrounded by peri-tubular dentin (PTD), embedded in a matrix of inter-tubular dentin (ITD). The PTD and the ITD have different relative fractions of collagen and hydroxyapatite crystals. The ITD is typically less rigid than the PTD, which can be seen as a set of parallel hollow cylindrical reinforcements in the ITD matrix. In this paper, we extend Hashin and Rozen's homogenization scheme to a non-uniform distribution of hollow PTD cylinders, determined from image analysis. We relate the transverse isotropic elastic coefficients of a

Representative Elementary Volume (REV) of dentin to the elastic and topological properties of PTD and ITD. The model is calibrated against experimental data. Each sample tested is consistently characterized by Environmental Scanning Electron Microscopy (ESEM), nano-indentation and Resonant Ultrasound Spectroscopy (RUS), which ensures that macroscopic mechanical properties measured are correlated with microstructure observations. Despite the high variability of microstructure descriptors and mechanical properties, statistical analyses show that Hashin's bounds converge and that the proposed model can be used for back-calculating the microscopic Poisson's ratios of dentin constituents. Three-point bending tests conducted in the laboratory were simulated with the Finite Element Method (FEM). Elements were assigned transverse isotropic elastic parameters calculated by homogenization. The tubule orientation and the pdf of the ratio inner/outer tubule radius were determined in several zones of the beams before testing. The remainder of the micro-mechanical parameters were taken equal to those calibrated by RUS. The horizontal strains found experimentally by Digital Image Correlation (DIC) were compared to those found by FEM. The DIC and FEM horizontal strain fields showed a very good agreement in trend and order of magnitude, which verifies the calibration of the homogenization model. By contrast with previous studies of dentin, we fully calibrated a closed form mechanical model against experimental data and we explained the testing procedures. In elastic conditions, the proposed homogenization scheme gives a better account of microstructure variability than micro-macro dentin models with periodic microstructure.

Keywords: dentin; homogenization model; microstructure imaging; three-point bending tests; Finite Element Method

1. Introduction

Most restorations of dental cavities do not last more than 15 years, a limitation which raised interest in the micro-macro mechanical modeling of dentin, their main anchorage tissue. Dentin is indeed the main tissue of the tooth, located between the pulp and the enamel [1]. If assumed isotropic, its overall Young's modulus ranges between 12 GPa (close to the pulp) and 20 GPa (close to the enamel) [2,3,4,5]. Many studies [6,7,8] show that dentin is mechanically anisotropic, however. Structurally, dentin can be seen as a bundle of hollow fibers of peri-tubular dentin (PTD) embedded in a matrix of inter-tubular dentin (ITD). The Young's moduli of PTD and ITD are in the order of 30-45 GPa and 15-25 GPa, respectively [9,10].

Dentin, like bone, is mainly made of hydroxyapatite crystals and collagen fibrils. In bone, collagen is organized in different lamellae (surrounding the haversian canals of the osteonal unit) of parallel fibrils [11], hence bone ultrastructure is anisotropic. Dentin exhibits distinct zones of PTD and ITD. PTD is mainly made of mineral and ITD is an entanglement of organic and mineral features. According to the dentin literature, ITD is quasi-isotropic [10]. And as hydroxyapatite crystals are randomly oriented in PTD [12], PTD can also be considered quasi-isotropic.

In bone, the absence of tubules makes it possible to represent a Representative Elementary Volume (REV) of bone as a matrix/inclusion system and to use Eshelby's theory to relate the mechanical properties of the bone tissue to those of its constituents. For instance, a two-step homogenization procedure was employed to understand the mineral-collagen interactions in bone ultrastructure [13]. The REV is a porous matrix that contains hydroxyapatite and water inclusions. The porous

matrix is itself a composite, represented as a solid matrix made of hydroxyapatite crystal that contains long ellipsoidal collagen inclusions. More general homogenization schemes comprising five to six steps were formulated to model different types of bone tissues [14,15,16].

In dentin, tubules cannot be considered as convex inclusions, because they go through the entire REV. The rigorous calculation of the stiffness coefficients of a solid with hollow cylinder inclusions is not trivial. Hashin and Rosen [17] computed exact bounds in the case of a hexagonal pattern of fibers, assuming *a priori* that the homogenized material was transverse isotropic. Improvements were then made by Hervé and Zaoui [18], Hongjun [19], Shi [20] and Tsukrov [21]. Due to their complexity, these models were never used to back analyze the mechanical properties of dentin constituents. Previous studies of dentin homogenized properties were based on Reuss and Voigt bounds [22], the self-consistent method [23], averaging techniques assuming periodic structure [24] and Hashin and Rosen bounds [25]. None of these models was verified experimentally and the values of the microscopic Poisson's ratios had to be postulated instead of being calibrated. By contrast, we establish a stiffness homogenization scheme based on microstructure images and mechanical datasets. In the first section, we describe the materials and experimental methods employed. Secondly, we explain how to link the microscopic and macroscopic anisotropic properties of dentin by using Hashin's homogenization scheme with a non-uniform distribution of PTD volume around the tubules, determined from image analysis. In the third section, we calibrate the proposed stiffness model against nano-indentation tests and Resonant Ultrasound Spectroscopy (RUS) measurements. Lastly, we verify the homogenization model against the displacement field obtained by Digital Image Correlation (DIC) during three-point bending tests.

2. Experimental protocols

2.1. *Materials*

Three human wisdom teeth (third molars) were used in this study. To avoid bacterial infections, teeth were immersed in Chloramine-T at 0.5% for one week, before being stored in a Ringer's solution, an isotonic solution that is close to fluids in the buccal environment. Most of the enamel of the crown was polished off, to allow machining on a plane surface and to avoid damaging the drill bit in the enamel. The teeth were then embedded in Plexcil epoxy resin and glued to a support especially designed to be used in a 4-axis milling center (Lyra prototype; GACD SASU). Dentin beams for three-point bending tests were prepared at URB2i (Paris Descartes University, France) on a 4-axis machining center equipped with a cylindrical diamond KaVo tool (d = 2 mm). Water lubrication was employed to avoid any damage in dentin microstructure that could have occurred due the increase of temperature during machining. In each tooth, we extracted horizontal and vertical dentin beams, as shown in Figure 1. The face of the beam closest to the enamel was polished for

microstructure characterization by Environmental Scanning Electron Microscopy (ESEM), see Subsection 2.2. Beam dimensions measured after polishing are reported in Table 1.

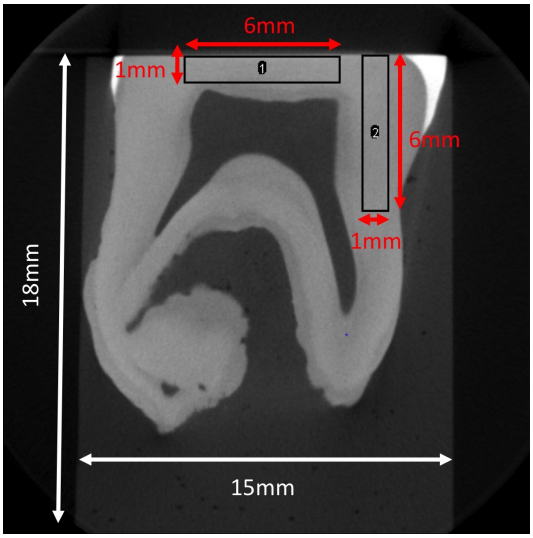

Fig. 1. Micro-tomographic image of one of the teeth collected in this study. The tooth was polished to remove most of the enamel at the top. Two beams of dentin were extracted from each tooth, close to the enamel.

Table 1. Dimensions of the dentin beam samples tested in three-point bending.

Sample	Length (x-dir.) (mm)	Width (y-dir) (mm)	Height (z-dir) (mm)
D1	5.20	0.88	0.88
D2	5.80	0.83	0.80
D3	5.85	0.90	0.80

2.2. *Environmental Scanning Electron Microscopy (ESEM)*

ESEM microstructure images were obtained with a *Quanta* 600 (FEI Co., USA) at Laboratoire de Mécanique du Solide (LMS, Ecole Polytechnique, France). Figure 2 shows an ESEM image of dentin, taken in a horizontal tooth section. The ITD is made of collagen and apatite and forms a matrix that contains fluid-filled tubules surrounded by PTD, mostly made of apatite [37]. Tubules are between 2.9 μm and 3.02 μm in diameter and the tubule density is between 18,200 fibers/mm^2 and

24,100 fibers/mm^2 [38]. The surface concentration of tubules is higher close to the pulp than to the enamel, because tubules spread out forming a fan. In the following, we propose a homogenization scheme for a dentin REV, at the scale of which tubules can be considered parallel (Fig.3). The numerical analyses presented in Subsection 3.3 show that the REV should contain 60 tubules (or truncated tubules) minimum, which corresponds to an elementary volume of the order of $1.66 \times 10^5 \mu m^3$.

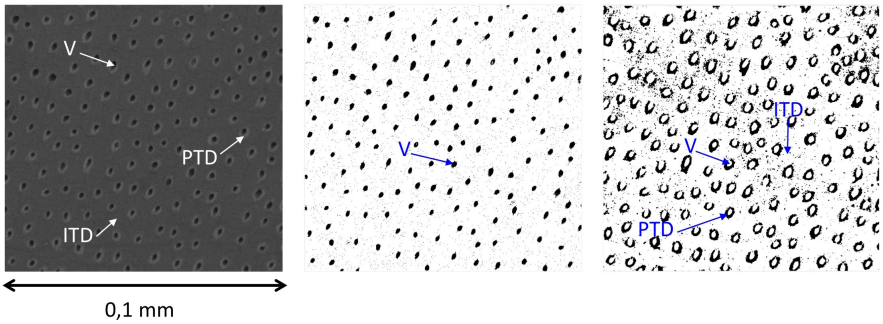

Fig. 2. ESEM image of dentin (left) taken in a horizontal plane of the tooth. Binarized image (middle), showing the voids (V) in black. Filtered binarized image (right), showing the PTD in black.

To determine the probability density function (pdf) of the ratio inner/outer tubule radius (noted α), we obseved 1,186 fibers in 6 ESEM images. We modeled the pdf of α as a truncated Gaussian distribution, varying between 0.2 and 0.8 (see Figure 4):

$$\rho(\alpha) = \frac{1}{\sqrt{2\pi}\sigma} \cdot e^{-\frac{(\mu_\alpha - \alpha)^2}{2\sigma_\alpha^2}} \tag{1}$$

In which μ_α and σ_α are the mean and standard deviation of the pdf $\rho(\alpha)$, respectively. The averaged error between the pdf obtained by image analysis and the fitted pdf is 15% (acceptable, provided the variability of biological parameters). To find the volume fraction of ITD (noted v_m), we analyzed 24 images of dentin in cross-sections located at different elevations in the tooth. As explained above, the large difference of tubule surface density between sections close to the pulp and sections close to the enamel results in a great variance. In the following, we take the average value of v_m for the calculations. Microstructure statistical analyses are summarized in Table 2.

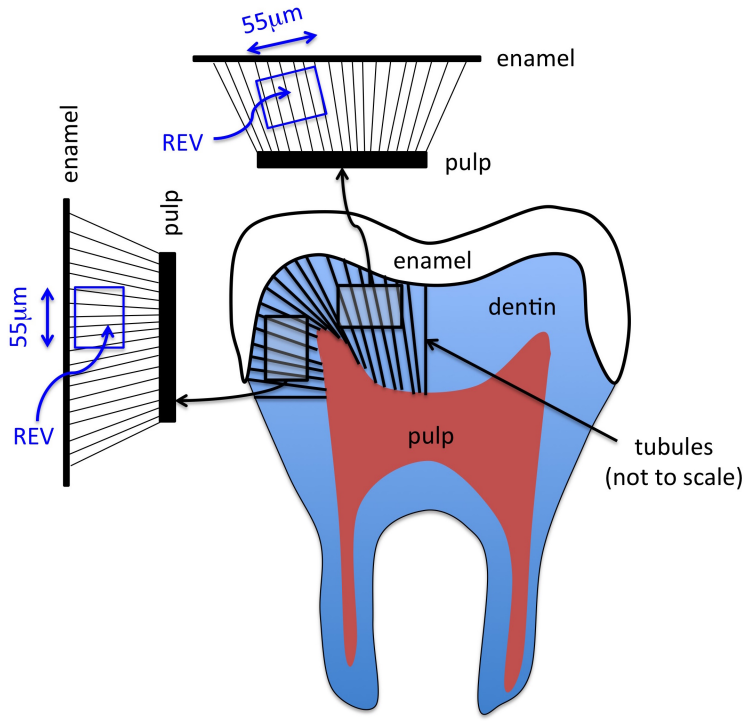

Fig. 3. Schematic view of the REV of dentin considered in the homogenization model. Tubules spread out forming a fan. The REV is of the order of $55\mu m \times 55\mu m \times 55\mu m = 1.66 \times 10^5 \mu m^3$ and contains 60 truncated tubules.

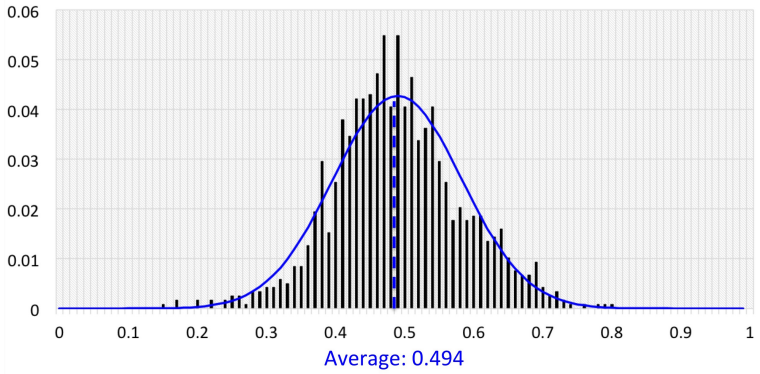

Fig. 4. Probability density function of the ratio inner radius / outer radius (parameter α), obtained by image analysis.

Table 2. Results of dentine image analysis. SD: Standard Deviation.

α determination				v_m determination			
Average	SD	Min	Max	Average	SD	Min	Max
0.494	0.093	0.150	0.790	0.750	0.075	0.600	0.860

2.3. *Nano-indentation and Resonant Ultrasound Spectroscopy (RUS)*

The Young's moduli of ITD and PTD were obtained by nano-indentation [10] at MSSMat Laboratory (Centrale Supélec, France). RUS [26] measures were obtained at LIB (Paris VI University, France). The nano-indentation and RUS results are reported in detail in Wenlong Wang's Ph.D. thesis [27] and are summarized in Table 3 and Table 4, respectively.

Table 3. Young's moduli of ITD and PTD obtained by nano-indentation.

Nanoindentation	
E_{ITD} (GPa)	E_{PTD} (GPa)
18.46	31.08

Table 4. Dentin mechanical properties obtained by RUS.

Resonant ultrasound spectroscopy				
E_1 (GPa)	E_2 (GPa)	ν_{12}	ν_{23}	G_{12} (GPa)
23.35	21.9	0.298	0.512	9.63

Note: E_1, E_2: longitudinal, transversal Young's modulus (in the direction parallel, perpendicular to the tubules); ν_{12}, ν_{23}: out-of-plane, in-plane Poisson's ratio; G_{12}: out-of-plane shear modulus

The nano-indentation campaign consisted in producing over 100 indents in 9 dentin beams. The indentation depth was 200 nm, the strain rate for loading/unloading was 0,05 s^{-1} and the holding period was 10 s. Atomic Force Microscopy was used to distinguish indents located in ITD from those located in PTD. The method of Oliver and Pharr [28] was used to calculate the Young's modulus at each indent. The nano-indentation moduli reported in Table 3 are the average values of the moduli calculated at the ITD and PTD indents. A statistical indentation method borrowed from Hellmich's group [29,30,31] was used to quantify the non-uniformity of the Young's moduli of ITD and PTD. The method allows representing the Young's moduli by cumulative distribution functions (cdfs). One of the key assumptions of the statistical nano-indentation method is that it is possible

to reconstruct the cumulative distribution of moduli found experimentally by a superposition of Gausssian cdfs. In the samples used in this study, it was not always possible to distinguish two distribution modes. Hence, we used the scalar values reported in Table 3 to describe the Young's moduli of ITD and PTD. Details are provided in Appendix A.

In RUS, samples are subjected to vibrations of various frequencies, until an eigenfrequency is reached. Stiffness coefficients are calculated from those eigenfrequencies [32]. In the tests used in this study, frequencies ranged between 0.5 MHz and 1.4 MHz. RUS differs from ultrasonic tests in which waves are propagated through the sample at a fixed frequency, in various directions of space. In such ultrasonic tests, the material's moduli are back-calculated from the wave velocities after waves have traversed the sample, and it is necessary to ensure that the wavelength be larger than the sample size [14].

2.4. *Three-point bending tests*

Three-point bending tests were performed on the beams described in Table 1, using a *Shimadzu* testing machine with a 500 N load cell (precision of ± 1%). "Trapezium" software was used to process the data and plot the load and displacement of the crosshead as functions of time. The imposed crosshead speed was 1 mm/min until the load applied reached 0.1 N. After that, the imposed crosshead speed was 0.1 mm/min, until failure was reached. Figure 5 shows the experimental set up.

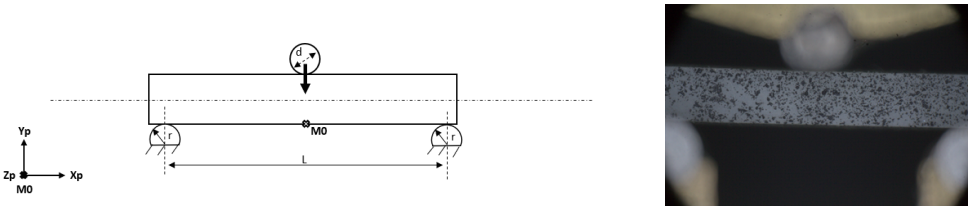

Fig. 5. Experimental set-up for three-point bending tests. Left: Dimensions (L = 5mm; r = 0.5mm; d = 1mm) and orientation: M0 (0,0) is the origin of the coordinate system Rp (Xp, Yp, Zp) linked to the beam. Right: Photograph of one of the beams during the test. The face shown was speckled for subsequent Digital Image Correlation, see Subsection 2.5.

2.5. *Digital Image Correlation (DIC)*

The polished face of the beam was speckled by means of an *Iwata* High Performance BP airbrush. We used India ink, which does not vanish when the beam is put back in Ringer's solution for storage. The diameter of the droplets was inferior to 50

μm. The speckled face was imaged by time-lapse photography during the three-point bending tests. Images were taken by a Reflex 60D camera (ISO = 1200 and exposure time = 1/80 s) with a resolution of 2061 x 1733 pixels every 3 s, starting 5 s after the beginning of the test, up until the complete failure of the sample. The camera was fixed to a *Questar* long-distance microscope QM 100 installed on a tripod. The set up is shown in Figure 6.

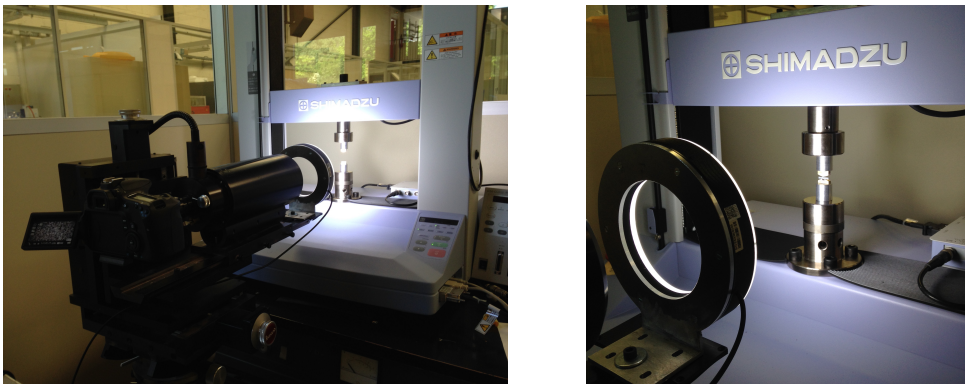

Fig. 6. Experimental set-up for time-lapse micro-photography during three-point bending tests.

DIC was invented at the beginning of the 80s to calculate 2D or 3D displacement and strain fields by means of a referent image and a deformed image [33]. The method can be used to determine mechanical properties of homogeneous materials [34]. In this study, DIC was done with *CorreliQ4* software, which has the advantage of reconstructing the displacement and strain fields by using the same shape functions as in the Finite Element Method (FEM) [35]. Displacement and strain fields are calculated over a Region of Interest (ROI) selected by the user. Each pixel of the ROI is linked to a gray level. Under the assumption of continuity of the displacement field, any sub-element of the ROI, called Zone of Interest (ZOI), has the same texture in the referent and deformed images. *CorreliQ4* divides the ROI into ZOIs in the referent image, correlates them with the ZOIs in the deformed image and finally calculates the displacements and strains by comparing the positions of the points of the referent and deformed ZOIs [36]. Figure 7 explains the principle of DIC.

We calculated displacement and strain fields for various ZOI sizes (16, 32, 64 and 128 pixels) and found that for a ZOI of 64 pixels in size or more, the strain field obtained by DIC did not exhibit extreme gradients over the ROI. The precision of the DIC technique with ZOIs larger than 64 pixels (or $110\mu m$) is thus satisfactory to assess the validity of the numerical model. In what follows, we use 64-pixel-ZOIs, for which the *a priori* displacement uncertainty is 1.2 x 10^{-3} pixels or 2 x 10^{-3} μm.

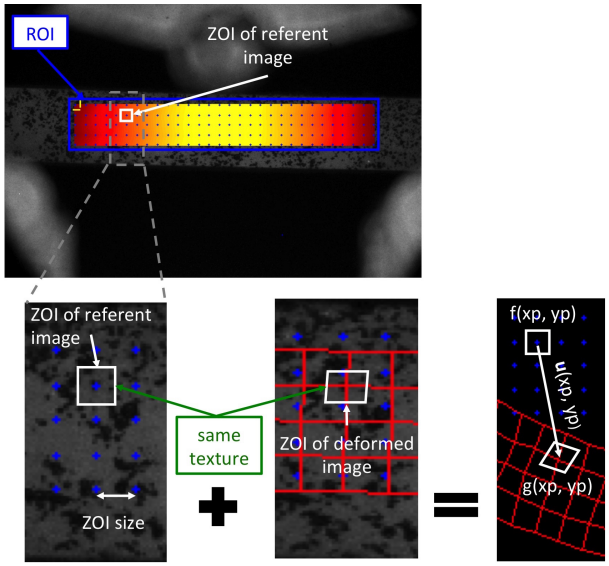

Fig. 7. Principle of Digital Image Correlation (DIC). *CorreliQ4* DIC software monitors displacement fields (u) by means of gray levels that are assigned to each pixel of the Zone of Interest (ZOI) by dedicated functions (f for the pixels of the referent image and g for the pixels of the deformed image)

3. Homogenization Scheme

3.1. *Stiffness of a solid containing a random distribution of hollow cylinders (Hashin's model)*

We consider a dentin REV, in which the ITD matrix contains randomly distributed hollow cylinders (tubules surrounded by PTD), all oriented along direction 1. Assuming that the ITD, PTD and pore fluids are isotropic linear elastic, the mechanical behavior of the dentin REV is transverse isotropic linear elastic. Using Voigt notation, the stiffness matrix of the dentin REV is expressed as:

$$\begin{Bmatrix} \epsilon_{11} \\ \epsilon_{22} \\ \epsilon_{33} \\ 2\epsilon_{12} \\ 2\epsilon_{13} \\ 2\epsilon_{23} \end{Bmatrix} = \begin{bmatrix} \frac{1}{E_1} & \frac{-\nu_{12}}{E_1} & \frac{-\nu_{12}}{E_1} & 0 & 0 & 0 \\ \frac{-\nu_{12}}{E_1} & \frac{1}{E_2} & \frac{-\nu_{23}}{E_2} & 0 & 0 & 0 \\ \frac{-\nu_{12}}{E_1} & \frac{-\nu_{23}}{E_2} & \frac{1}{E_2} & 0 & 0 & 0 \\ 0 & 0 & 0 & \frac{1}{G_{12}} & 0 & 0 \\ 0 & 0 & 0 & 0 & \frac{1}{G_{12}} & 0 \\ 0 & 0 & 0 & 0 & 0 & \frac{2(1+\nu_{23})}{E_2} \end{bmatrix} \begin{Bmatrix} \sigma_{11} \\ \sigma_{22} \\ \sigma_{33} \\ \sigma_{12} \\ \sigma_{13} \\ \sigma_{23} \end{Bmatrix} \tag{2}$$

in which E_1 is the longitudinal Young's modulus, E_2 is the transversal Young's modulus, ν_{12} is the out-of-plane Poisson's ratio, ν_{23} is the in-plane Poisson's ratio and G_{12} is the out-of-plane shear modulus. We first assume that the ratio α is

uniform in the REV. We use the energy-based method proposed by Hashin and Rosen [17] to find bounds for the five independent macroscopic elastic parameters E_1, E_2, ν_{12}, ν_{23} and G_{12}.

The strain energy stored in the REV minimizes the strain energy that can be stored under any statically admissible displacement or stress field. If a displacement field is prescribed at the REV's boundary, the macroscopic strain field $\overline{\boldsymbol{\epsilon}}$ is known and a statically admissible macroscopic stress field $\boldsymbol{\sigma}$ can be found, for which the stiffness tensor $\mathbf{C}$ of the REV satisifies:

$$W_u = \frac{1}{2}\overline{\boldsymbol{\epsilon}} : \mathbf{C} : \overline{\boldsymbol{\epsilon}} \leq \frac{1}{2}\boldsymbol{\sigma} : \overline{\boldsymbol{\epsilon}} \tag{3}$$

In the same way, if a stress field $\overline{\boldsymbol{\sigma}}$ is prescribed at the REV's boundary, a statically admissible macroscopic strain field $\boldsymbol{\epsilon}$ can be found, for which the compliance tensor $\mathbf{S}$ of the REV satisifies:

$$W_\sigma = \frac{1}{2}\overline{\boldsymbol{\sigma}} : \mathbf{S} : \overline{\boldsymbol{\sigma}} \leq \frac{1}{2}\overline{\boldsymbol{\sigma}} : \boldsymbol{\epsilon} \tag{4}$$

Equations 3 and 4 provide upper and lower bounds of the stiffness coefficients of the REV, respectively. In transerve isotropy, statically admissible stress and displacement fields need to be expressed for five independent loading conditions. Hashin and Rosen proposed analytical solutions for:

- The problem of lateral confinement under zero axial loading, to bound the lateral bulk modulus K_{23};
- The problem of out-of-plane shear loading (directions 1-2), to bound the out-of-plane shear modulus G_{12};
- The problem of axial loading under zero lateral confinement, to bound the axial Young's modulus E_1;
- The problem of in-plane shear loading (directions 2-3), to bound the in-plane shear modulus G_{23};
- The problem of oedometric loading with axial loading and fixed lateral boundaries, to bound the stiffness coefficient C_{11}.

The five elastic parameters E_1, E_2, ν_{12}, ν_{23} and G_{12} in Eq. 2 can be expressed in terms of the five elastic coefficients K_{23}, G_{12}, E_1, G_{23} and C_{11} by using the following relationships:

$$\nu_{12} = \frac{1}{2}\left(\frac{C_{11} - E_1}{K_{23}}\right)^{1/2} \tag{5}$$

$$\nu_{23} = \frac{K_{23} - \psi\, G_{23}}{K_{23} + \psi\, G_{23}} \tag{6}$$

$$E_2 = \frac{4K_{23}\, G_{23}}{K_{23} + \psi\, G_{23}} \tag{7}$$

where $\psi = 1 + 4K_{23}\nu_{12}^2/E_1$.

For a random distribution of parallel hollow cylinders that all have the same ratio α, the lower and upper bounds of K_{23}, G_{12}, E_1 and C_{11} are equal, and their expressions are given below. For the lateral bulk modulus:

$$K_{23}^{+} = K_{23}^{-} = \overline{K}_{ITD} \frac{\phi(1-\alpha^2)(1+2\nu_{ITD}(1-v_m)) + \left(1+\frac{\alpha^2}{2\nu_{PTD}}\right) 2\nu_{ITD} v_m}{\phi(1-\alpha^2)v_m + \left(1+\frac{\alpha^2}{2\nu_{PTD}}\right)(1-v_m+2\nu_{ITD})} \tag{8}$$

in which $\phi = \overline{K}_{PTD}/\overline{K}_{ITD}$ and $\overline{K}_{ITD}$ and $\overline{K}_{PTD}$ stand for the plane-strain bulk moduli of ITD and PTD, respectively. For the out-of-plane shear modulus:

$$G_{12}^{+} = G_{12}^{-} = G_{ITD} \frac{\eta(1-\alpha^2)(2-v_m) + (1+\alpha^2)v_m}{\eta(1-\alpha^2)v_m + (1+\alpha^2)(2-v_m)} \tag{9}$$

in which $\eta = G_{PTD}/G_{ITD}$ and G_{ITD} and G_{PTD} are stand for the shear moduli of ITD and PTD, respectively. For the axial Young's modulus:

$$E_1^{+} = E_1^{-} = E_{ITD}\left(v_f \frac{E_{PTD}}{E_{ITD}+v_m}\right) \frac{E_{ITD}(D_1 - D_3F_1) + E_{PTD}(D_2 - D_4F_2)}{E_{ITD}(D_1 - D_3) + E_{PTD}(D_2 - D_4)} \tag{10}$$

in which v_f is the volume fraction of PTD: $v_f = (1-\alpha^2)(1-v_m)$, and in which:

$$D_1 = \frac{1+\alpha^2}{1-\alpha^2} - \nu_{PTD} \tag{11}$$

$$D_2 = \frac{2-v_m}{v_m} + \nu_{ITD} \tag{12}$$

$$D_3 = \frac{2\nu_{PTD}^2}{1-\alpha^2} \tag{13}$$

$$D_4 = 2\nu_{ITD}^2 \frac{1-v_m}{v_m} \tag{14}$$

$$F_1 = \frac{\nu_{ITD} v_f E_{PTD} + \nu_{PTD} v_m E_{ITD}}{\nu_{PTD} v_f E_{PTD} + v_m E_{ITD}} \tag{15}$$

$$F_2 = \frac{\nu_{PTD}}{\nu_{ITD}} F_1 \tag{16}$$

For the stiffness coefficient C_{11}:

$$C_{11}^{+} = C_{11}^{-} = E_1^{+} + 4\nu_{12}^2 K_{23}^{+} \tag{17}$$

in which E_1^{+} and K_{23}^{+} are calculated from Eq. 10 and 8, respectively, and in which:

$$\nu_{12} = \frac{v_f E_{PTD} L_1 + v_m E_{ITD} L_2 \nu_{ITD}}{v_f E_{PTD} L_3 + v_m E_{ITD} L_2} \tag{18}$$

where:

$$L_1 = 2\nu_{PTD}(1-\nu_{ITD}^2)(1-v_m) + v_m(1+\nu_{ITD})\nu_{ITD} \tag{19}$$

$$L_2 = (1-v_m)\left[(1+\nu_{PTD})\alpha^2 + 1 - \nu_{PTD} - 2\nu_{PTD}^2\right] \tag{20}$$

$$L_3 = 2(1-\nu_{ITD}^2)(1-v_m) + (1+\nu_{ITD})v_m \tag{21}$$

For a random distribution of parallel hollow cylinders that all have the same ratio α, only G_{23} has two distinct bounds, expressed as:

$$G_{23}^{+} = G_{ITD}\left[1 - \frac{2(1-\nu_{ITD})}{1-2\nu_{ITD}}(1-v_m)A_\epsilon\right] \tag{22}$$

$$G_{23}^{-} = \frac{G_{ITD}}{\left[1 - \frac{2(1-\nu_{ITD})}{1-2\nu_{ITD}}(1-v_m)A_\sigma\right]} \tag{23}$$

in which A_ϵ and A_σ are two constants that have to be determined by solving a complex system of equations, detailed in the appendix of the original paper by Hashin and Rosen [17].

3.2. *Extension of Hashin's model to cylinders with a non-uniform ratio inner/outer radius*

In the original model of Hashin and Rosen, hollow cylinders are aligned and have a circular cross section characterized by the same ratio inner radius / outer radius (noted α). In this work, the non-uniform distribution of α is modeled by a truncated Gaussian law and α varies between 0.2 and 0.8 (see Table 2 and Figure 4). The homogenized stiffness coefficients $\overline{C_{ij}}$ thus satisfy:

$$\frac{1}{\overline{\rho}}\int_{\alpha=0.2}^{\alpha=0.8}\rho(\alpha)C_{ij}^{-}(\alpha)d\alpha \leq \overline{C_{ij}} \leq \frac{1}{\overline{\rho}}\int_{\alpha=0.2}^{\alpha=0.8}\rho(\alpha)C_{ij}^{+}(\alpha)d\alpha \tag{24}$$

with:

$$\overline{\rho} = \int_{\alpha=0.2}^{\alpha=0.8}\rho(\alpha)d\alpha \tag{25}$$

in which $C_{ij}^{-}(\alpha)$ and $C_{ij}^{+}(\alpha)$ are Hashin's lower and upper bounds of the stiffness coefficient C_{ij} for a given value α. Consequently, the proposed homogenization scheme requires seven microscopic parameters: the Young's moduli (E_{ITD}, E_{PTD}) and the Poisson's ratios (ν_{ITD}, ν_{PTD}) of ITD and PTD, the volume fraction of ITD (v_m) and the statistical parameters of the pdf of α (μ_α, σ_α).

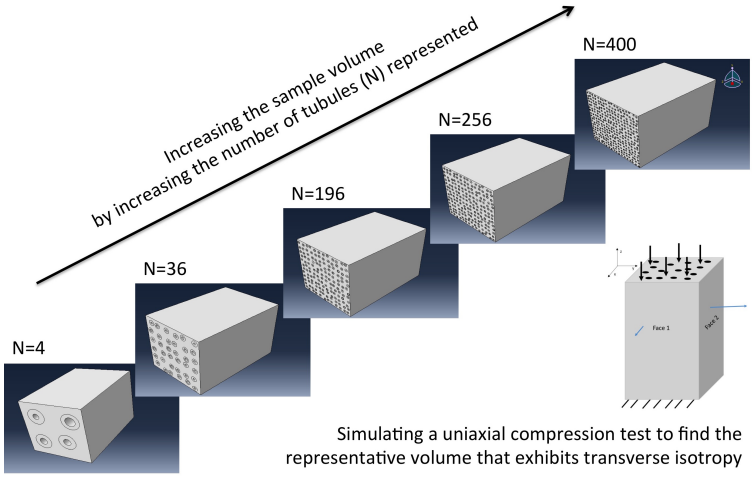

Fig. 8. FEM models used to simulate strain-controlled compression tests. The load was applied along the x-axis (direction of the tubules) and the transverse displacements on orthogonal faces were calculated.

3.3. *Representative Elementary Volume (REV)*

We used the FEM to simulate the mechanical response of dentin subjected to a strain-controlled uniaxial compression imposed along the axis of the tubules. Numerical samples were parallelepipedic with 4 to 400 parallel hollow cylinders of circular section and same external radius. The hollow cylinders representing the tubules were assigned a random distribution of α, which determined the inner radius distribution. Tubules were placed on rectangular and hexagonal grids, with a random distribution of offsets along the x and y directions. In total, 20 FEM models were tested for each of the two patterns (Figure 8). Results for hexagonal and rectangular patterns are plotted in Figure 9. The difference between transverse displacements on opposite vertical faces decreases with the number of cylinders, and then stabilizes at around 2% for samples with 60 cylinders or more, for both hexagonal and rectangular patterns. This means that the assumption of transverse isotropy is valid for dentin samples containing 60 tubules or more, i.e. REV dimensions should be at least 55 μm in each direction of space. For a volume of that size, it is reasonable to assume that PTD hollow cylinders are parallel (See Figures 2 and 3).

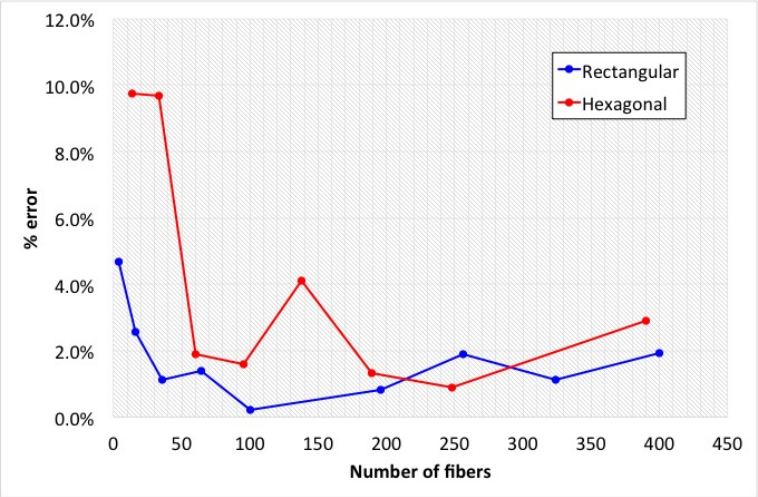

Fig. 9. Difference between transverse displacements on opposite vertical faces of the FEM models used for REV determination. A small error on the displacements indicates that the assumption of transverse isotropy is valid, and that the FEM domain is a REV. Simulations were done with tubule centroids placed on rectangular and hexagonal patterns.

4. Model Calibration

4.1. *Convergence of Hashin's Bounds*

Hashin's bounds are equal for E_1, E_2, G_{12} and ν_{12} (see Section 3.1). In order to check the suitability of our model to homogenize dentin properties, we verified that the bounds of the transverse shear modulus G_{23} converge for the range of values taken by the seven microstructure parameters of dentin. We used a genetic algorithm to find the maximum difference between the two bounds of G_{23} (noted Δ_{G23}^{max}) under the following constraints: the Young's moduli of the ITD and PTD are assigned the values found by nano-indentation (Table 3); the Poisson's ratios of ITD and PTD vary between 0 and 0.5; v_m ranges between 0.6 and 0.86, according to image analyses (Table 2); the pdf of α is that found by image analysis and the range of values taken by α is divided into seven intervals, between 0.2 and 0.8. We calculated the maximum difference beween the two bounds of the transverse shear modulus on that interval (noted E_i for the i-th interval). The average of this maximum difference was calculated as:

$$\Delta_{G23}^{max} = \int_{0.2}^{0.8} \rho(\alpha) \times e(\alpha) d\alpha, \quad e(\alpha) = E_i \in [a_i^{min}; a_i^{max}] \tag{26}$$

In which $[a_i^{min}; a_i^{max}]$ designates the i^{th} of the seven subintervals used for the discretized calculation of the bounds difference. We tested the optimization technique

for four ranges of values $[a_1^{min}; a_7^{max}]$ (and adapted the seven subintervals accordingly). The corresponding values of E are provided in Table 5. The overall upper bound for Δ_{G23}^{max} is equal to 24.1 %. Note that the values of the Poisson's ratios were fixed on each interval, and that the discretization was coarse (only seven intervals). Thus the optimization method employed in this study overpredicts errors. A maximum difference of 24.1% in the bounds of the shear modulus is thus considered acceptable.

Table 5. Maximum difference between the bounds of the transverse shear modulus for various ranges of values of α.

Interval for α	[0.2; 0.8]	[0.3; 0.7]	[0.4; 0.6]	[0.45; 0.55]
E_i (%)	79	41	19	13

4.2. *Back calculation of microscopic Poisson's ratios*

Note that RUS, nano-indentation and ESEM were performed on the same samples, which ensured consistency between the measures used for calibration in the following. We found the microscopic Poisson's ratios of ITD and PTD (ν_{ITD} and ν_{PTD}) by fitting the macroscopic elastic parameters of dentin against measures obtained by RUS, under the constraint that E_{ITD}, E_{PTD}, μ_{v_m}, μ_α and σ_α take the values determined by image analysis and nano-indentation (Tables 2 and 3). Using * and *Hashin* superscripts to refer to RUS measures and model predictions respectively, we define the following fitness function F_1:

$$\begin{aligned} &F_1(\nu_{ITD}, \nu_{PTD}) = \frac{1}{7}[\textstyle\sum_\Gamma \Delta_\Gamma + \delta_{G23} + \delta_{stat}] \\ &\Delta_\Gamma = \frac{|\Gamma^{Hashin}(\nu_{ITD},\nu_{PTD}) - \Gamma^*|}{\Gamma^*}, \quad \Gamma = E_1,\, E_2,\, \nu_{12},\, G_{12},\, G_{23} \\ &\delta_{stat} = \frac{max(\Delta_\Gamma) - min(\Delta_\Gamma)}{max(\Delta_\Gamma)}, \quad \delta_{G23} = \frac{G_{23}^{max} - G_{23}^{min}}{G_{23}^{min}} \end{aligned} \tag{27}$$

Since the transverse shear modulus is characterized by two bounds, $\Delta_{G_{23}}$ is taken equal to the relative error between $G_{23}*$ and the closest bound, and to 0 if $G_{23}*$ is within the bounds found numerically. We used a genetic algorithm to minimize F_1 and find the values of the ITD and PTD Poisson's ratios that best fit experimental data in the range [0.05; 0.5]. The parameter δ_{stat} is used to balance the optimization criteria between the five macroscopic elastic properties, and δ_{G23} is introduced to put more weight on the solutions for which the two bounds of the shear modulus are close. δ_{stat} and δ_{G23} regularize the fitness function F_1 (they are assigned the same weight in our study). The optimization was done over a maximum of 500 generations of 100 individuals. The iterative optimization process was stopped when the best individuals did not vary over 20 generations. We found $\nu_{ITD} = 0.381$ and $\nu_{PDT} = 0.344$. The corresponding value of the fitness function was 18% and the

maximum difference between the two bounds of the transverse shear modulus was 0.23%. The relative errors for the macroscopic elastic parameters were the following: $\Delta_{E_1} = 14\%$; $\Delta_{E_2} = 14\%$; $\Delta_{\nu_{12}} = 13\%$; $\Delta_{G_{12}} = 26\%$; $\Delta_{G_{23}} = 22\%$.

5. Model Verification

5.1. *Simulation of three-point bending tests by the FEM*

We simulated the three-point bending tests described in Section 2.4 with *ABAQUS* FEM software. The geometry of the beam was the same as in the experiment. We used 8-node linear brick elements, with reduced integration (one integration point) and hourglass control. The mesh and boundary conditions are shown in Figure 10(a). The two supports and the indenter were modeled as rigid bodies. The supports were fixed whereas the indenter was subjected to a vertical displacement determined from DIC measurements. We only simulated the experiments before failure, for small displacements.

Beam samples were imaged prior to the three point bending tests to determine the pdf of the parameter α and the orientation of the tubules. The methodology that we followed to find the orientation angles is described in detail in Appendix B. Since the samples presented a high tubule orientation variability, we divided the FEM domain into subdomains that were 0.25 mm thick and that each represented a zone of the beam where the tubules have a similar orientation (Figure 10(b)). A transverse isotropic linear elastic model was assigned to all elements. For each zone of the beam, direction 1 was defined as the tubule axial direction. We used the homogenization model presented in Section 3 to calculate the five parameters E_1, E_2, ν_{12}, ν_{23} and G_{12} from the orientation of the tubules (determined before the tests), the value of v_m (Table 2), the pdf of α (determined before the tests) and the Young's moduli and Poisson's ratios of PTD and ITD (Table 3 and Section 4.2). Provided the two orientation angles of the tubules, two rotation operators were then applied to obtain the stiffness matrix of the dentin elements in the (x,y,z) plane. Figure 16 in Appendix B summarizes the micro-macro parameters used in each zone of the FEM model, for each of the three beams tested. As an example, Figure 11 shows the displacement and stress maps obtained by FEM at two stages of the three-point bending test for sample D1.

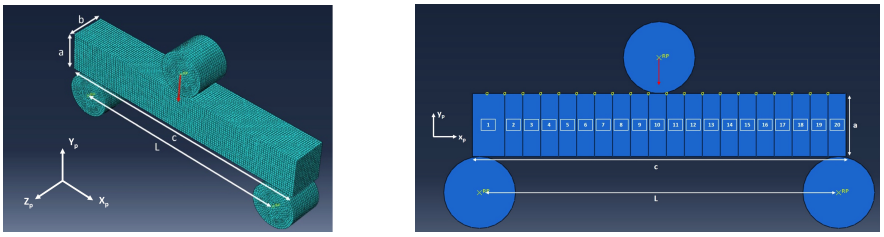

(a) FEM mesh and boundary conditions (D1). (b) Zones with similar tubule orientation (D1).

Fig. 10. FEM model used to simulate the three-point bending tests. L = 5mm; a: beam height, b: beam width; c: beam length.

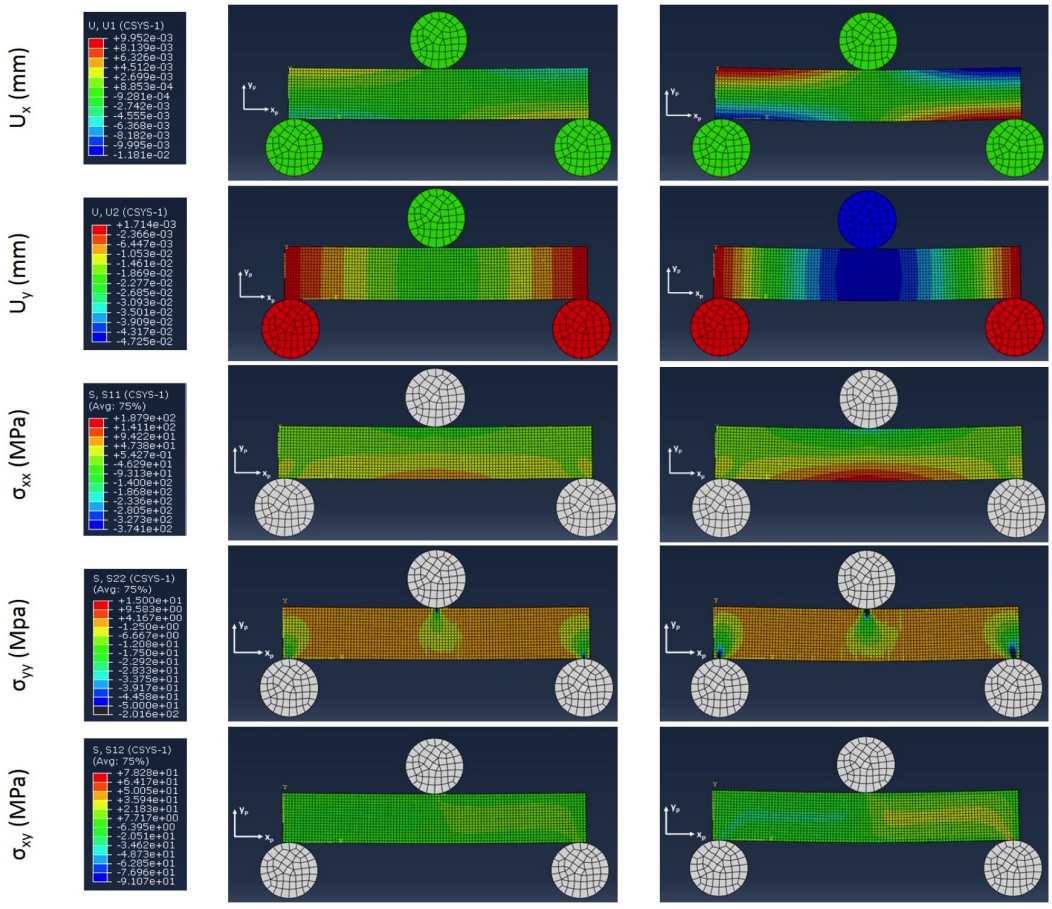

Fig. 11. FEM displacement and stress maps obtained for beam D1 during the three-point bending test after applying half of the maximum load (left) and the full maximum load, just before failure (right)

5.2. *Results and discussion*

The total displacement measured by DIC is the sum of the rigid body motion of the entire beam, which occurs because of the displacements of the experimental set-up, and of the displacement induced by bending deformation. The supports being outside of the ROI, the rigid body motion of the supports could not be directly measured by DIC. Hence, we calculated the deflection at the bottom of the beam within the ROI, and we extrapolated it to estimate the vertical displacement of the supports (x = ±2.5 mm). The latter was subtracted from the total displacements of the ZOIs to remove the rigid body motion, as explained in Figure 12.

Figure 13 shows a comparison between the horizontal strain fields obtained by FEM and those obtained by DIC for each beam. The vertical displacements applied on the indenter were 0.047 mm, 0.066 mm and 0.077 mm for beams D1, D2 and D3, respectively. The resultant force reached just before failure on the indenter were 15.95 N for beam D1, 14.42 N for beam D2 and 21.51 N for beam D3. The corresponding forces calculated in the FEM were very similar: 14.37 N for beam D1, 16.52 N for beam D2 and 21.13 N for beam D3. Because of speckle defects, noise was observed in the DIC results and it was not possible to compare the numerical and experimental strain fields point by point (or ZOI by ZOI). Despite this resolution limitation, we note in Figure 13 that the horizontal strains are of the same order of magnitude over the entire ROI, for each beam tested. The maximum tensile strain at the bottom of the beam is of the order of 5×10^{-3} for beam D1, 8×10^{-3} for beam D2 and 10×10^{-3} for beam D3. The maximum compressive strain at the top of the beam is of the order of -7×10^{-3} for beam D1, -10×10^{-3} for beam D2 and -13×10^{-3} for beam D3. A strain close to zero is observed at mid-height of the beams, close to the neutral axis.

The proposed homogenization scheme is appropriate for capturing the anisotropic elastic behavior of dentin. Its formulation requires only 7 microstructure parameters, plus the orientation of the tubules. All of these model parameters can be obtained experimentally through ESEM imaging and nano-indentation, or back-calculated from macroscopic mechanical measurements, e.g., by RUS. Model predictions are more precise than Reuss and Voigt bounds presented in former studies. Assumptions are more realistic than in the self-consistent method (in which there is no concept of matrix, i.e. ITD, PTD and tubules are interwoven inclusions) or in periodic microstructure models (which disregard the heterogeneity of tubule and PTD space distributions). Compared to analytical homogenization schemes for composites reinforced by hollow fibers of finite length, the proposed model can easily be implemented in a computer code for calibration and FEM simulations. The modified Hashin's model is thus a rigorous model that can be used to back-calculate dentin microstructure parameters and to simulate loading paths on a tooth with the FEM, without meshing each dentin constituent individually. Applications of the elastic dentin model at the scale of an entire tooth will be presented in future work to compare the mechanical behavior of healthy, damaged and restored tissues.

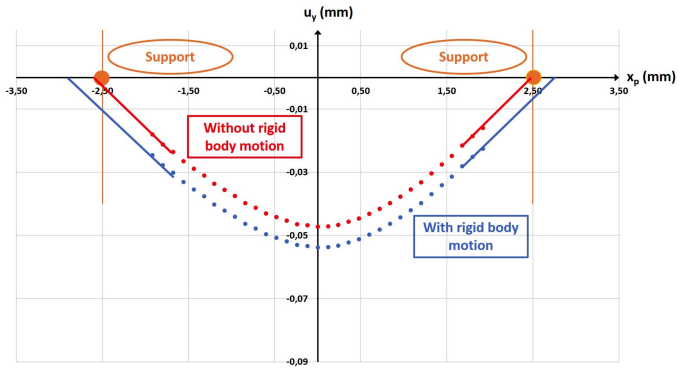

Beam D1

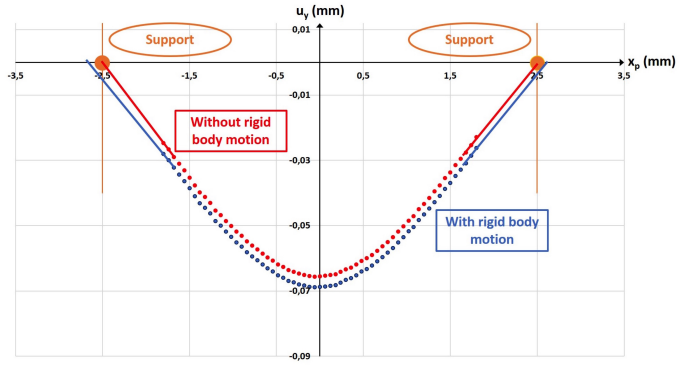

Beam D2

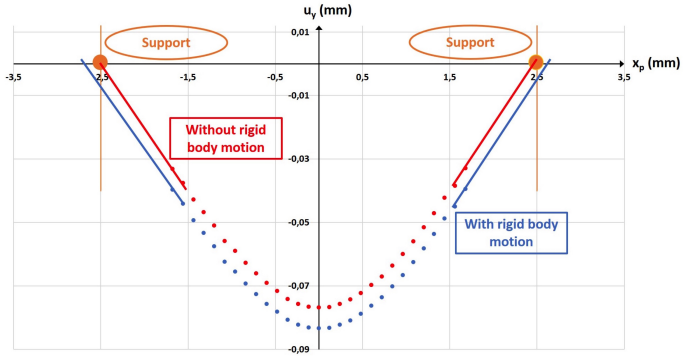

Beam D3

Fig. 12. Removal of the rigid body deflection from the vertical displacements obtained by DIC: (i) Calculation of the total deflection at the bottom of the beams by DIC; (ii) Extrapolation of the deflection curve to the supports; (iii) Subtraction of the difference of the deflection at the supports from the total deflection obtained by DIC.

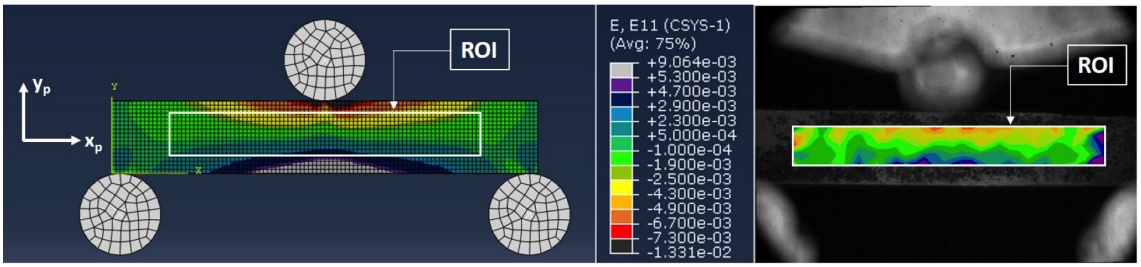

Beam D1, u_y=0.047 mm

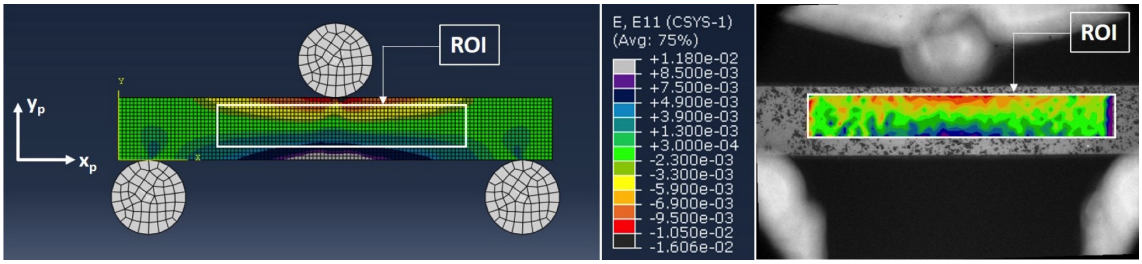

Beam D2, u_y=0.066 mm

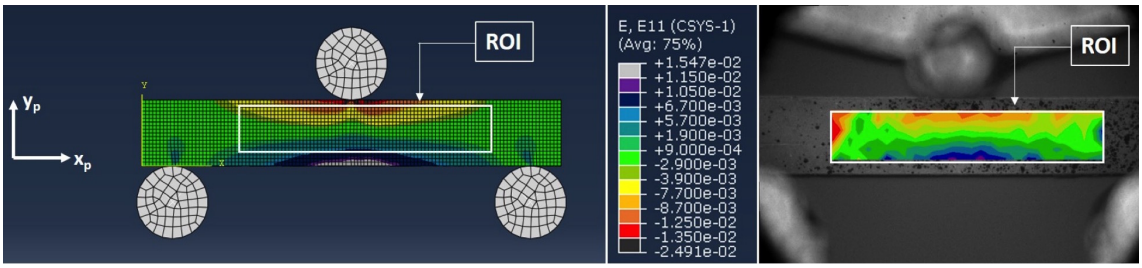

Beam D3, u_y=0.077 mm

Fig. 13. Comparison of the horizontal strain fields obtained by FEM (left) and by DIC (right).

6. Conclusions

Restorative materials used to fill teeth cavities are anchored in dentin. State-of-the-Art micro-macro models of dentin rely on simplified microstructure representations and lack experimental verification. Moreover, the Poisson's ratios of dentin microstructure components cannot be easily determined experimentally. In this study, we model dentin as a bundle of parallel hollow cylinders made of tubules surrounded by Peri-Tubular Dentin (PTD), embedded in a matrix of Inter-Tubular Dentin (ITD). By contrast with previous modeling approaches, we establish a homogenization scheme for a non-uniform distribution of PTD, determined from image analysis. The minimum size of the Representative Elementary Volume is a cube containing 60 tubules. ESEM, nano-indentation and RUS data were collected from each dentin sample studied for model calibration, which is unprecedented. Statistical analyses show that Hashin's bounds converge and that the proposed model can be used for back-calculating the microscopic mechanical properties of dentin constituents, in particular the most probable values of the Poisson's ratios of ITD and PTD. Three-point bending tests were conducted on dentin beams of about 5.5 mm in length. One face of each beam was polished and speckled. That face was photographed at regular time intervals with a reflex camera connected to a *Questar* long-distance microscope. Digital Image Correlation was used to track the displacement fields on the photographed face during the tests. After removing the rigid body motion displacements of the beams, the horizontal strains found by DIC were compared to those found by simulating the three-point bending tests with the proposed homogenization model, by the FEM. In the numerical models, elements were assigned transverse isotropic elastic parameters calculated by homogenization. The tubule orientation and the pdf of the ratio inner/outer tubule radius were determined in several zones of the beams before testing. The remainder of the micro-mechanical parameters were taken equal to those calibrated by RUS. The DIC and FEM horizontal strain fields showed a very good agreement in trend and order of magnitude, which verifies the calibration of the homogenization model. In future work, the proposed homogenization model will be used in a 3D numerical model of tooth to study the influence of the location, size and shape of empty and restored cavities on the mechanical response of dentin under compression.

Acknowledgments

The first author was funded by Université Paris-Saclay (bourse d'Alembert: "Micro-macro mechanical modeling of teeth with cavities restored by resin-based techniques", Arson and Vennat, 2017-2018). This work benefited from the financial support of the LabeX LaSIPS (ANR-10-LABX-0040-LaSIPS) managed by the French National Research Agency under the "Investissements d'avenir" program (ANR-11-IDEX-0003-02). Funding for this research was also provided by Ecole Centrale de Paris through the bourse de mobilité étudiante for Romain Jeanneret. The au-

thors express their gratitute to Stéphane Le Goff at URB2i for helping with sample preparation, Chloé Giraudet at LMS for assisting with sample preparation and ink spraying, Tanguy Alexandre and Simon Hallais at LMS for bringing technical support with ESEM, and Lofti Slimani at URB2i for helping with CT scanning.

Appendix A. Statistical nano-indentation method

For each nano-indentation measurement, the method of Oliver and Pharr [28] was used to relate the reduced modulus E_r to the elastic unloading stiffness S, defined as the slope of the unloading curve at the initial stage of unloading:

$$S = \frac{2}{\sqrt{\pi}} E_r \sqrt{A} \tag{A.1}$$

in which A is the contact area. The reduced elastic modulus E_r is expressed as:

$$\frac{1}{E_r} = \frac{(1-{\nu_i}^2)}{E_i} + \frac{(1-{\nu_s}^2)}{E_s} \tag{A.2}$$

in which the properties of the diamond indenter are known: $E_i = 1,141\,GPa$, $\nu_i = 0.07$. The Young's modulus of the phase indented, E_s, is found by assuming that the Poisson's ratio of that phase, ν_s, is known. Here, it is assumed that $\nu_s = 0.4$, which is the average value of the Poisson's ratio of the dentin samples found by RUS. Noting $E_{s,i}$ the Young's modulus at indent i, the experimental Cumulative Distribution Functions (cdfs) of E_s for one sample was calculated as:

$$D_{exp}\left(E_{s,i}\right) = \frac{i}{N} - \frac{1}{2N} \tag{A.3}$$

in which $i \in [1, N]$, $N > 100$ being the number of indents per sample, and the values of the measured $E_{s,i}$ are sorted in ascending order. In the statistical nano-indentation method followed by Hellmich's group [29,30,31], it is assumed that $D_{exp}\left(E_{s,i}\right)$ can be approximated by the superposition of several Gaussian cdfs $D\left(E_{s,i}, \mu_j, s_j\right)$ such that:

$$D\left(E_{s,i}, \mu_j, s_j\right) = \frac{1}{s_j\sqrt{2\pi}} \int_{-\infty}^{E_i} exp\left(\frac{-(u-\mu_j)^2}{2{s_j}^2}\right) du \tag{A.4}$$

in which μ_j and s_j are the mean value and the standard deviation of the j^{th} cdf, respectively. The number of phases, M, and the means μ_j and standard deviations s_j are found by minimizing the following difference d for various trial values of M:

$$d = \sum_{i=1}^{N} \left(\sum_{j=1}^{M} f_j D\left(E_{s,i}, \mu_j, s_j\right) - D_{exp}\left(E_{s,i}\right) \right)^2 \tag{A.5}$$

in which the f_j scalars are weighting factors that satisfy the partition of unity:

$$\sum_{j=1}^{M} f_j = 1 \tag{A.6}$$

In our present study, M is known and set equal to 2. Figure 14 below presents statistical analyses performed on two different samples. In Figure 14(a), two modes can clearly be distinguished: for ITD (phase 1), $\mu_1 = 18.66\,GPa$, $s_1 = 3.6\,GPa$; for PTD (phase 2): $\mu_2 = 33.36\,GPa$, $s_2 = 4.9\,GPa$. For Figure 14(b), only one mode can be identified, and we can only measure the properties of ITD: $\mu_1 = 15.94\,GPa$, $s_1 = 1.8\,GPa$. In the second sample, the number of indents is too small to characterize both phases. Therefore, we used Atomic Force Microscopy to locate the position of the indents. The nano-indentation moduli reported in Table 3 for ITD and PTD are the average values of the moduli found in ITD and PTD over the 9 samples indented.

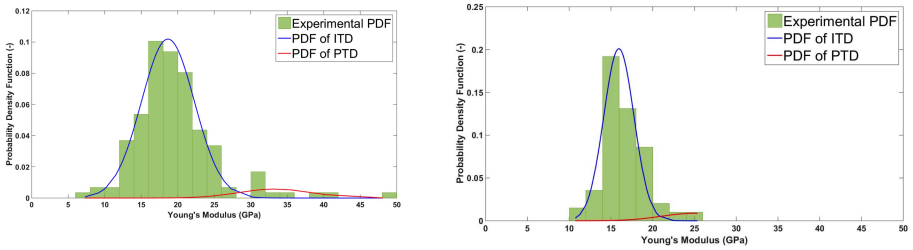

(a) Nano-indentation sample 1: two modes. (b) Nano-indentation sample 2: one mode.

Fig. 14. Statistical nano-indentation method applied to two dentin beams subjected to over 100 indents each.

Appendix B. Microstructure parameters used in the FEM simulations

In a 3D space, tubule orientation depends on two angles that can be found by analyzing one microstructure image only. Considering an ESEM image taken on the polished face of the beam tested in three-point bending, we note $(\boldsymbol{x_p}, \boldsymbol{y_p}, \boldsymbol{z_p})$ the coordinate system relative to the beam, and $(\boldsymbol{x_e}, \boldsymbol{y_e}, \boldsymbol{z_e})$ that of an ellipse seen in the micrograph (See Figure 15). The angle β between $\boldsymbol{x_p}$ and $\boldsymbol{x_e}$ can be measured directly from the images. Ellipses represent the trace of the cylindrical tubules on the plane of the ESEM image. We note $(\boldsymbol{x_t}, \boldsymbol{y_t}, \boldsymbol{z_t})$ the coordinate system of the tubule (See Figure 15). Noting θ the angle between $\boldsymbol{z_e}$ and $\boldsymbol{z_t}$, we have:

$$\begin{aligned} \boldsymbol{x_t} &= cos\theta\, \boldsymbol{x_e} - sin\theta\, \boldsymbol{z_e} \\ \boldsymbol{y_t} &= \boldsymbol{y_e} \\ \boldsymbol{z_t} &= sin\theta\, \boldsymbol{x_e} + cos\theta\, \boldsymbol{z_e} \end{aligned} \tag{B.1}$$

In addition, the Cartesian equation of the cylinder is:

$$\frac{(x_t)^2}{R^2} + \frac{(y_t)^2}{R^2} = 1 \tag{B.2}$$

in which R is the radius of the circular cross-section of the tubule. At $z_e = 0$, we have $x_t = cos\theta\, x_e$. Introducing the expression of x_t into Equation B.2, we have:

$$\frac{(x_e)^2\,(cos\theta)^2}{R^2} + \frac{(y_e)^2}{R^2} = 1 \tag{B.3}$$

The equation of the ellipse is:

$$\frac{(x_e)^2}{a^2} + \frac{(y_e)^2}{b^2} = 1 \tag{B.4}$$

therefore, by identification:

$$a = \frac{R}{cos\theta}, \quad b = R \tag{B.5}$$

The dimensions of the ellipse (a, b) can be found from image analyses, and the angle θ is then calculated with Equation B.5. Microstructure parameters for each zone of each beam tested are reported in Figure 16.

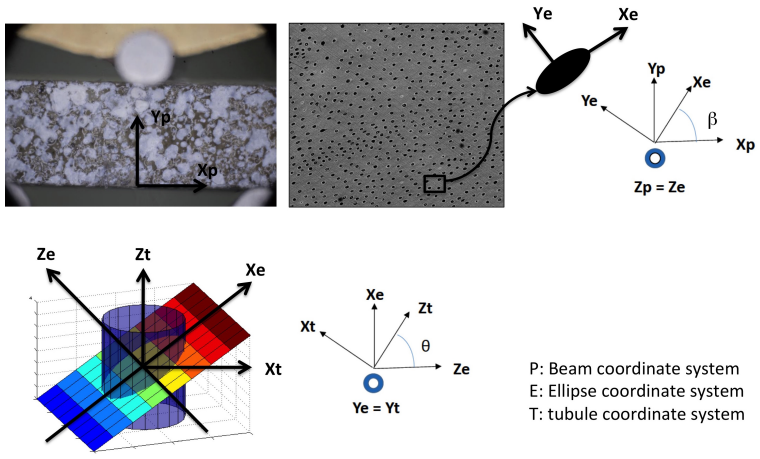

Fig. 15. Method to determine the orientation of the tubules in 3D from only one ESEM image.

Beam D1

Zone	Beta (°)	Theta (°)	E_1 (GPa)	$E_2 = E_3$ (GPa)	$\nu_{12} = \nu_{13}$ (-)	ν_{23} (-)	$G_{12} = G_{13}$ (GPa)	G_{23} (GPa)
1	32	69	19.052	14.962	0.467	0.312	6.037	5.701
2	32	69	19.052	14.962	0.467	0.312	6.037	5.701
3	32	69	19.052	14.962	0.467	0.312	6.037	5.701
4	35	68	19.648	15.321	0.481	0.296	6.247	5.909
5	44	66	19.408	15.033	0.477	0.308	6.119	5.747
6	48	64	18.833	14.633	0.464	0.325	5.901	5.522
7	53	64	18.476	14.395	0.456	0.335	5.773	5.390
8	53	66	19.052	14.710	0.470	0.321	5.962	5.566
9	57	65	18.878	14.626	0.466	0.325	5.907	5.519
10	67	65	18.360	14.304	0.454	0.339	5.727	5.342
11	67	65	17.630	13.810	0.437	0.359	5.467	5.079
12	62	66	18.784	14.674	0.462	0.324	5.906	5.543
13	61	63	19.210	15.178	0.468	0.304	6.124	5.821
14	63	63	18.761	14.827	0.459	0.318	5.946	5.623
15	65	62	18.314	14.531	0.449	0.331	5.785	5.460
16	86	58	18.381	14.553	0.451	0.330	5.803	5.472
17	89	58	17.781	14.168	0.437	0.346	5.596	5.264
18	93	57	18.275	14.539	0.448	0.331	5.782	5.463
19	96	58	18.028	14.370	0.442	0.338	5.693	5.372
20	91	57	18.045	14.536	0.440	0.331	5.746	5.459

Beam D2

Zone	Beta (°)	Theta (°)	E_1 (GPa)	$E_2 = E_3$ (GPa)	$\nu_{12} = \nu_{13}$ (-)	ν_{23} (-)	$G_{12} = G_{13}$ (GPa)	G_{23} (GPa)
1	44	60	17.215	13.497	0.427	0.372	5.315	4.918
2	42	60	18.230	14.225	0.450	0.342	5.684	5.298
3	39	57	17.709	13.967	0.437	0.353	5.525	5.160
4	39	55	18.898	14.865	0.463	0.316	5.981	5.646
5	39	54	17.365	13.984	0.426	0.353	5.479	5.167
6	39	52	18.829	14.773	0.462	0.320	5.942	5.595
7	38	51	17.497	14.152	0.428	0.347	5.550	5.253
8	38	50	17.997	14.635	0.437	0.328	5.769	5.511
9	38	49	18.434	14.954	0.447	0.315	5.930	5.686
10	36	49	18.853	15.256	0.456	0.303	6.089	5.856
11	37	48	17.708	14.725	0.427	0.325	5.747	5.558
12	39	48	19.003	15.498	0.457	0.293	6.181	5.992
13	46	48	17.720	14.605	0.429	0.329	5.714	5.494
14	48	45	18.481	15.370	0.442	0.299	6.053	5.916
15	49	45	18.396	15.323	0.440	0.301	6.025	5.889
16	44	42	18.578	15.491	0.443	0.294	6.101	5.984
17	47	43	19.021	15.713	0.454	0.285	6.241	6.114
18	53	45	18.774	15.441	0.451	0.296	6.124	5.958
19	62	44	18.384	15.222	0.441	0.305	5.996	5.833
20	68	44	17.355	14.480	0.419	0.334	5.620	5.427
21	83	46	17.555	14.447	0.426	0.335	5.642	5.410
22	95	47	17.524	14.480	0.424	0.334	5.647	5.427
23	109	52	18.263	14.693	0.445	0.325	5.824	5.545

Beam D3

Zone	Beta (°)	Theta (°)	E_1 (GPa)	$E_2 = E_3$ (GPa)	$\nu_{12} = \nu_{13}$ (-)	ν_{23} (-)	$G_{12} = G_{13}$ (GPa)	G_{23} (GPa)
1	140	43	21.476	17.042	0.511	0.224	7.072	5.899
2	141	42	21.406	17.006	0.510	0.226	7.049	5.878
3	138	40	21.785	17.218	0.518	0.216	7.183	6.003
4	136	38	20.637	16.652	0.491	0.244	6.798	5.675
5	135	39	21.714	17.181	0.516	0.218	7.158	5.981
6	137	40	21.334	16.997	0.507	0.227	7.031	5.872
7	133	42	20.194	16.372	0.482	0.256	6.638	5.522
8	127	42	20.249	16.432	0.482	0.254	6.664	5.554
9	120	42	19.911	16.224	0.475	0.263	6.544	5.443
10	116	46	19.438	15.928	0.464	0.276	6.376	5.288
11	125	46	19.452	15.932	0.465	0.276	6.380	5.290
12	118	46	18.986	15.611	0.455	0.289	6.208	5.126
13	111	47	17.930	14.958	0.430	0.316	5.848	4.810
14	115	47	18.750	15.528	0.448	0.293	6.144	5.087
15	125	46	19.653	16.087	0.469	0.269	6.458	5.370
16	132	49	18.330	15.263	0.439	0.303	5.998	4.957
17	128	51	18.627	15.482	0.445	0.295	6.109	5.065
18	122	52	17.775	14.828	0.427	0.321	5.786	4.748
19	123	52	17.959	14.958	0.431	0.316	5.853	4.810
20	119	54	17.978	14.844	0.434	0.320	5.824	4.752
21	117	54	17.387	14.511	0.419	0.333	5.636	4.600
22	114	51	16.743	13.868	0.407	0.358	5.352	4.306
23	123	53	16.825	14.232	0.405	0.343	5.469	4.480

Fig. 16. Micro-macro mechanical parameters used for each of the zones of the FEM model, for each of the three beams tested in three-point bending.

References

1. C.H. Lloyd and S.N. Scrimgeour et al. Dental materials : 1993 literature review. *Journal of Dentistry*, 23(2):67–93, 1995.
2. E Mahoney, A Holt, M Swain, and N Kilpatrick. The hardness and modulus of elasticity of primary molar teeth: an ultra-micro-indentation study. *Journal of dentistry*, 28(8):589–594, 2000.
3. L. Angker, M.V. Swain, and N. Kilpatrick. Micro-mechanical characterisation of the properties of primary tooth dentine. *Journal of dentistry*, 31(4):261–267, 2003.
4. W. Fränzel and R. Gerlach. The irradiation action on human dental tissue by x-rays and electrons–a nanoindenter study. *Zeitschrift für Medizinische Physik*, 19(1):5–10, 2009.
5. YL Chan, AHW Ngan, and NM King. Nano-scale structure and mechanical properties of the human dentine–enamel junction. *Journal of the mechanical behavior of biomedical materials*, 4(5):785–795, 2011.
6. T. Inoue, H. Takahashi, and F. Nishimura. Anisotropy of tensile strengths of bovine dentin regarding dentinal tubule orientation and location. *Dental materials journal*, 21(1):32–43, 2002.
7. JH Kinney, SJ Marshall, and GW Marshall. The mechanical properties of human dentin: a critical review and re-evaluation of the dental literature. *Critical Reviews in Oral Biology & Medicine*, 14(1):13–29, 2003.
8. RK Nalla, JH Kinney, and RO Ritchie. Effect of orientation on the in vitro fracture toughness of dentin: the role of toughening mechanisms. *Biomaterials*, 24(22):3955–3968, 2003.
9. G Balooch, GW Marshall, SJ Marshall, OL Warren, SA Syed Asif, and M Balooch. Evaluation of a new modulus mapping technique to investigate microstructural features of human teeth. *Journal of biomechanics*, 37(8):1223–1232, 2004.
10. D. Ziskind, M. Hasday, S.R. Cohen, and H.D. Wagner. Young's modulus of peritubular and intertubular human dentin by nano-indentation tests. *Journal of structural biology*, 174(1):23–30, 2011.
11. J.Y. Rho, L. Kuhn-Spearing and P. Ziouposc. Mechanical properties and the hierarchical structure of bone. *Med Eng Phys*, 20:92–102, 1998.
12. L. Schroeder and R.M. Frank. High resolution transmission electron microscopy of adult human peritubular dentine. *Cell. Tissue Res.*, 242:449–451, 1985.
13. C. Hellmich, J.F. Barthélémy and L. Dormieux. Mineralcollagen interactions in elasticity of bone ultrastructurea continuum micromechanics approach. *European Journal of Mechanics-A/Solids*, 23(5):783–810, 2004.
14. A. Fritsch and C. Hellmich. 'Universal' microstructural patterns in cortical and trabecular, extracellular and extravascular bone materials: micromechanics-based prediction of anisotropic elasticity. *Journal of Theoretical Biology*, 244(4):597–620, 2007.
15. A. Fritsch, C. Hellmich and L. Dormieux. Ductile sliding between mineral crystals followed by rupture of collagen crosslinks: experimentally supported micromechanical explanation of bone strength. *Journal of Theoretical Biology*, 260(2): 230–252, 2009.
16. E. Hamed, Y. Lee and I. Jasiuk. Multiscale modeling of elastic properties of cortical bone. *Acta Mechanica*, 213(1–2):131–154, 2010.
17. Z. Hashin and B.W. Rosen. The elastic moduli of fiber-reinforced materials. *Journal of Applied Mechanics*, pages 223–235, jun 1964.
18. E. Herve and A. Zaoui. n-layered inclusion-based micromechanical modelling. *International Journal of Engineering Science*, 1993.
19. H. Xiang, Zhifei Shi, and T. Zhang. Elastic analyses of heterogeneous hollow cylin-

ders. *Mechanics Research Communications*, 33(33):681–691, 2006.
20. Z. Shi, T. Zhang, and H. Xiang. Exact solutions of heterogeneous elastic hollow cylinders. *Composite S*, 79:140–147, 2007.
21. I. Tsukrov and Borys Drach. Elastic deformation of composite cylinders with cylindrical orthotropic layers. *Solids and Structures*, 47:25–33, 2010.
22. J.L. Katz. Hard tissue as angle composite material - i. bounds on the elastic behavior. *Journal Biomechanics*, 4:455–473, 1971.
23. J.H Kinney, M. Balooch, G.W. Marshall, and S.J Marshall. A micromechanics model of the elastic properties of human dentine. *Archives of Oral Biology*, 44(44):813–822, 1999.
24. B. Bar-On and H.D. Wagner. Elastic modulus of hard tissues. *Journal of Biomechanics*, 45:672–678, 2012.
25. Q-H Qin and M.V. Swain. A micro-mechanics model of dentin mechanical properties. *Biomaterials*, 25:5081–5090, 2004.
26. J.H. Kinney, J.R. Gladden, G.W. Marshall, S.J. Marshall, J.H. So, and J.D. Maynard. Resonant ultrasound spectroscopy measurements of the elastic constants of human dentin. *Journal of Biomechanics*, 37:437–441, 2004.
27. W. Wang. *Caractérisation géométrique et mécanique multi-échelle de la dentine humaine*. PhD thesis, Paris Saclay, 2016.
28. W.C. Oliver, G.M. Pharr. An improved technique for determining hardness and elastic modulus using load and displacement sensing indentation experiments. *Journal of materials research*, 7(6):1564–1583, 1992.
29. H. Kariem, M.I. Pastrama, S.I. Roohani-Esfahani, P. Pivonka, H. Zreiqat and C. Hellmich. Micro-poro-elasticity of baghdadite-based bone tissue engineering scaffolds: a unifying approach based on ultrasonics, nanoindentation, and homogenization theory. *Materials Science and Engineering: C*, 46:553–564, 2015.
30. I. Furin, M.I. Pastrama, H. Kariem, K.W. Luczynski, O. Lahayne and C. Hellmich. A new Nanoindentation Protocol for identifying the elasticity of undamaged extracellular bone tissue. *MRS Advances*, 1(11):693–704, 2016.
31. M.I. Pastrama, R. Blanchard, J.G. Clement, P. Pivonka and C. Hellmich. Modal analysis of nanoindentation data, confirming that reduced bone turnover may cause increased tissue mineralization/elasticity. *Journal of the mechanical behavior of biomedical materials*, 84:217–224, 2018.
32. S. Bernard. Resonant ultrasound spectroscopy for the viscoelastic characterization of cortical bone. *Doctoral dissertation, Paris VI University*, 2014.
33. MA Sutton, WJ Wolters, WH Peters, WF Ranson, and SR McNeill. Determination of displacements using an improved digital correlation method. *Image and vision computing*, 1(3):133–139, 1983.
34. A. Lagarde. Advanced optical methods and applications in solids mechanics. Technical report, POITIERS UNIV (FRANCE), 1998.
35. A. Bouterf, S. Roux, F. Hild, G. Vivier, X. Brajer, E. Maire, and S. Meille. Damage law identification from full field displacement measurement: Application to four-point bending test for plasterboard. *European Journal of Mechanics-A/Solids*, 49:60–66, 2015.
36. F. Hild and S. Roux. Correliq4: A software for finite element displacement field measurements by digital image correlation. Technical report, LMT Cachan, 2008.
37. G.W. Marshall, S.J. Marshall, J.H. Kinney, and M. Balooch. The dentine substrate : structure and properties related to bonding. *Journal of Dentistry*, 25(6):441–458, 1997.
38. R. Schilke, J. A. Lisson, O. Bauss, and W. Geurtsen. Comparison of teh number and

diameter of dedentin tubules in human and bovine dentine buy scanning electron microscopic investigation. *Archives of oral Biology*, 45:355–361, 2000.